A New Framework for SAR Multitemporal Data RGB Representation: Rationale and Products

Donato Amitrano, Gerardo Di Martino, *Member, IEEE,* Antonio Iodice, *Senior Member, IEEE,* Daniele Riccio, *Fellow, IEEE,* and Giuseppe Ruello, *Member, IEEE*

This work has been published on
IEEE Transactions on Geoscience and Remote Sensing

Abstract

This paper presents the Multitemporal Adaptive Processing (MAP3) framework for the treatment of multitemporal Synthetic Aperture Radar (SAR) images. The framework is organized in three major activities dealing with calibration, adaptability and representation. The processing chain has been designed looking at the simplicity, i.e. the minimization of the operations needed to obtain the products, and at the algorithms availability in literature. Innovation has been provided in the cross-calibration step, which is solved introducing the Variable Amplitude Levels Equalization (VALE) method, through which it is possible to establish a common metrics for the measurement of the amplitude levels exhibited by the images of the series. Representation issues are discussed with an application-based approach, supported by examples regarding semi-arid and temperate regions in which amplitude maps and interferometric coherence are combined in an original way.

Index Terms

Multitemporal SAR, data fusion, data mining, RGB composition

I. Introduction

Remote-sensing technologies have a huge potential in environmental monitoring and constitute a powerful instrument for large-scale investigations and planning. In particular, synthetic aperture radar (SAR) sensors play a decisive role in this context due to their all-weather and all-time capability that, together with the actually available short revisit times, makes them very attractive to work with multitemporal series for the study of dynamic phenomena. The analysis of such data can be set in the frame of the image-fusion theory, introducing relevant challenges with regard to the extraction, representation, and interpretation of information.

In this paper we present the MAP3 framework for the definition of new multitemporal products whose information content is higher than the one of the individual grayscale images. The crucial point is the definition of a reliable processing which should allow:

- The achievement of a set of spatially, temporally and radiometrically comparable images [1];
- The best level of interaction between the user and the machine during the decisional phase.

As for the image comparability, despeckling, calibration and quantization are faced with both state-of-art and innovative techniques. In particular, the main innovation is introduced in the cross-calibration phase, faced with the Variable Amplitude Levels Equalization (VALE), as detailed in Section IV. As for the human-machine interaction, a multitemporal data series can be considered as a three-dimensional datum in which the dimensions are space and time. Hence, its presentation is a non-trivial issue, with non-unique solution. The choice of appropriate color image spaces is needed in order to obtain new products that are easy to interpret for human and automatic analysis.

In the past, the RGB composition has been widely used because it provides products easily interpretable by human inspection. A color composite image, integrating different information sources, could be a powerful instrument for a quick individuation of the changes occurred in the study area since it makes possible a more easily interpretable result with respect to the original grayscale images. In this paper, we propose a new criterion for RGB composition oriented to multitemporal analysis of rural areas.

In remote-sensing data-analysis literature, the necessity to define general and analyst-driven frameworks has been highlighted by various authors [2]–[4]. who expressed the need to focus the processing on the users' skills, making the mathematical rigor, though of fundamental importance, secondary to the analysis and interpretation process [3].

Many of the modern algorithms that process SAR data "through the optimization of mathematical criteria are often sub-optimal in the sense that the output image is cluttered/fuzzy/noisy, visually unpleasing" [3] and difficult to be interpreted by non-expert SAR users. Therefore, one of the aim of this work is to emphasize the human-computer interaction as a value, provided that the respective strengths - computational efficiency for computers and interpretation capability for humans are enhanced. This means that any image processing technique, although looking for the maximum degree of automation, should never overlook users capability of judgment and native intuition, as explained in [3] and [4].

The authors are with the Department of Electrical Engineering and Information Technology, University of Napoli Federico II, Via Claudio 21, 80125 Napoli, Italy. email {donato.amitrano@unina.it; gerardo.dimartino@unina.it; iodice@unina.it; dariccio@unina.it; ruello@unina.it}

There is a strong need to develop environments allowing users data mining without "knowing the operators needed to represent the image information content at signal level" [4]. In fact, the capacity to understand data is still rather limited, due to the incremental value of developing sophisticated data-analysis algorithms is counterbalanced by the difficulty of disseminating the knowledge required to use them effectively. Hence, it is critical that remotely sensed data become accessible to people who may have the data-access and the analytical ability but not necessarily the mathematical background to understand the physics that has generated the image [3].

Thus, an important task is to develop new methodologies to transform the computer from a machine used for running complicate algorithms into an interface for the communication with other people and machines. In other words, one of the urgent priorities is to model the information either at a semantic level or at an electromagnetic/physical level, privileging aspects that are often postposed to the development of the specific technique. The idea is to build a general framework, tracing the guidelines for the development of new products to be added the so-called Level 1 and Level 2 products proposed by the providers of SAR data and which should be easily managed by a large variety of users. This work is focused on the definition of such products which we name *Level 1α products*, since they can be thought as an intermediate level between the already available Level 1 (see Fig. 1) and Level 2 products. These products, unlike the generalist Level 1, are application-modeled due to the adaptive nature of the processing that generates them.

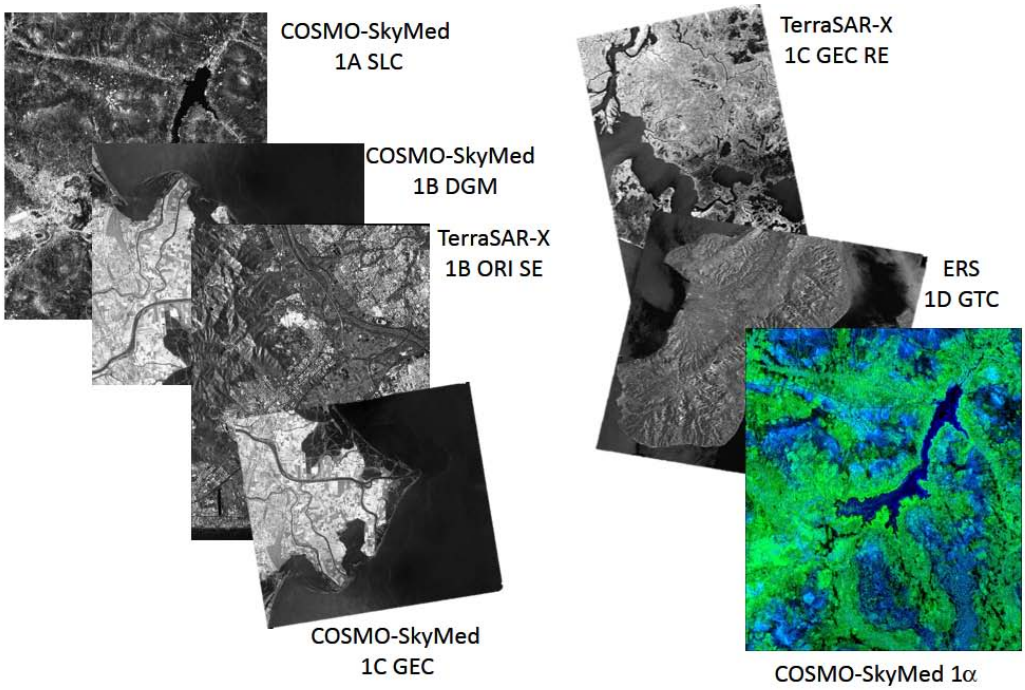

Fig. 1: Available Level 1 products, from 1A to 1α: SLC - Single Look Complex; DGM - Detected Ground projected Multilooked; ORI - Orthorectified Radar Image; GEC - Geocoded Ellipsoid Corrected; GTC - Geocoded Terrain Corrected; SE - Spatially Enhanced; RE - Radiometrically Enhanced.

The paper is organized as follows: in Section II we collect the previous literature about multitemporal SAR in order to identify its key aspects, the applications that exploited this technique, the weakness of the proposed solutions and the open points. Section III describes the general guidelines of the proposed framework and the processed datasets. Section IV deals with the pre-processing chain and calibration issues. Section V describes a possible application of the method, adapting its characteristics to the case of semi-arid regions. Section VI is devoted the RGB composition and the building of the new multitemporal products. Section VII highlights the independence of the framework from both the sensor and the imaged scene.

II. Previous representation concerning multitemporal SAR: categorization and rationale toward MAP3

The design of a new SAR multitemporal framework could not overlook the past literature. A systematic bibliographic study helped to properly collocate all the examined literature, and to identify the properties and characteristics to be taken into account in the building of the proposed products.

Multitemporal SAR data have been widely exploited in the development of techniques oriented to change detection, classification, segmentation and multisensor data fusion. Moreover, various authors have used multitemporal data to validate

empirical scattering models. References [5]–[7] use multitemporal SAR data to validate semi-empirical models for conifer-dominated forests response evaluation. Reference [8] studied the response of snow to estimate its water content and to extract classification maps. The problem of soil moisture retrieval has been studied in [9] and [10]. Empirical scattering models for crops growth monitoring have been developed in [11] and [12].

In the last decade, multitemporal SAR data have been often used for classification, segmentation, change detection, and land-cover-oriented applications, even with the use of data fusion techniques. Reference [13] proposes a technique for the fusion of multitemporal SAR data with a single multispectral datum for unsupervised classification purposes. Reference [14] also developed a multitemporal and multisource technique for classification and change detection. In [15] the authors use multitemporal SAR data for extracting segmentation maps. Classification-oriented applications have been developed in [16] and [17]. A lot of literature can be found dealing with change detection issues, either in rural or in urban areas [18]–[21]. Other applications involve feature extraction [22], with particular reference to roads, hydrological and agricultural monitoring [23] and studies on natural disasters, especially regarding floods [24]–[26] and fires [27].

Generally speaking, from the examined literature arises that a multitemporal SAR data processing technique should take into account the six key aspects listed below:

- Reproducibility: the processing chain should be transparent in all its steps;
- Automation: the techniques should be at minimal impact by the side of the user with the minimum number of parameters to be set up;
- Adaptability: the processing should be suitable for a large number of applications;
- Reversibility: the processing chain should preserve the electromagnetic and physics characteristics of the analyzed scene, giving rise to invertible models [28];
- Visualization: the output maps should be comfortable with human view and displayed in such a way to ease their interpretation [28];
- Interpretation: the obtained maps and value added products should be easily interpreted by a large variety of scientists and researchers belonging to different disciplinary sectors.

None of the examined works present all these properties. Adaptability is the major limitation for semi-empirical models such as [5]–[7], [11] and [12]. Inversion issues are faced only in [8]–[10], while all the other works are focused on the obtainment of vector maps, with limited attention to the retrieval of electromagnetic/physical characteristics of the scene. Actually, [25] proposes a more general technique, but the physical information of the data is compromised by the equalization processes.

Automation is a fundamental requirement for modern remotely sensed data processing techniques. As a matter of fact, all the examined works share a high degree of automation, although some of them require a training phase due to the use of neural networks [16]. Reproducibility, instead, is the weakness of many modern image processing algorithms, which are characterized by a great mathematical insight and few attention on the user experience.

Visualization and interpretation issues are faced only in [23], [29] and [25]. In particular, the latter performed a systematical study on this issue and solved it with the aid of RGB composition of channels suitable for flooding analysis.

The use of RGB composition in multitemporal SAR data analysis has been already presented in [23], [27], [29] and [30]. Reference [27] used the RGB composition to perform quantitative evaluation on the effects of fires in forests comparing successive SAR acquisitions in order to identify the more damaged areas and classify the damage. RGB compositions have been also exploited for the generation of land cover maps [26], [30] and for floods analysis. Reference [25] proposed a systematic study on the radar backscattering characteristics, supporting a robust and automatic technique for the study of flooding. In fact, as known, the backscattering coefficient is sensitive to the surface roughness, allowing efficient studies of flooding. Other applications which involve, for example, crop and vegetation, should take into account more complex scattering mechanisms, such as volumetric backscattering, and therefore need more refined models.

Dealing with multitemporal data, the radiometric calibration of the images involved in the processing is of central importance. As an example, COSMO-SkyMed single look products hold a radiometric accuracy smaller than 1 dB [31], [32] thanks to the internal calibration. This value could be improved through external calibration procedures, involving the use of active or passive calibrators, if available [33], [34], or through image-based techniques [35]. Indeed, the process of calibration of data is very delicate and could be affected by several sources of errors. For a complete discussion on this topic the reader should refer to [36].

III. Processed datasets and MAP3 workflow

The technique we propose for the elaboration of the new multitemporal products can be conveniently organized in three major blocks of activities, as conceptually shown in the block diagram of Fig. 2. The first block of activities involves the pre-processing chain in which data coregistration, despeckling and calibration issues are implemented. The second block concerns the adaptive processing in which the image combination that better emphasizes the relevant characteristics of the scene is chosen. Finally, the last block is relevant to representation and analysis. Because of the multitemporal and adaptive nature of the proposed framework, we named it MAP3 (Multitemporal Adaptive Processing), where the number three recalls the number of blocks. The design of the blocks was guided by the six properties listed in Section II and pointed to the simplicity,

minimizing the operations necessary to obtain the products, and to the availability of the algorithms, with the exception of the cross-calibration step, where we introduced a new technique presented in Section IV-C.

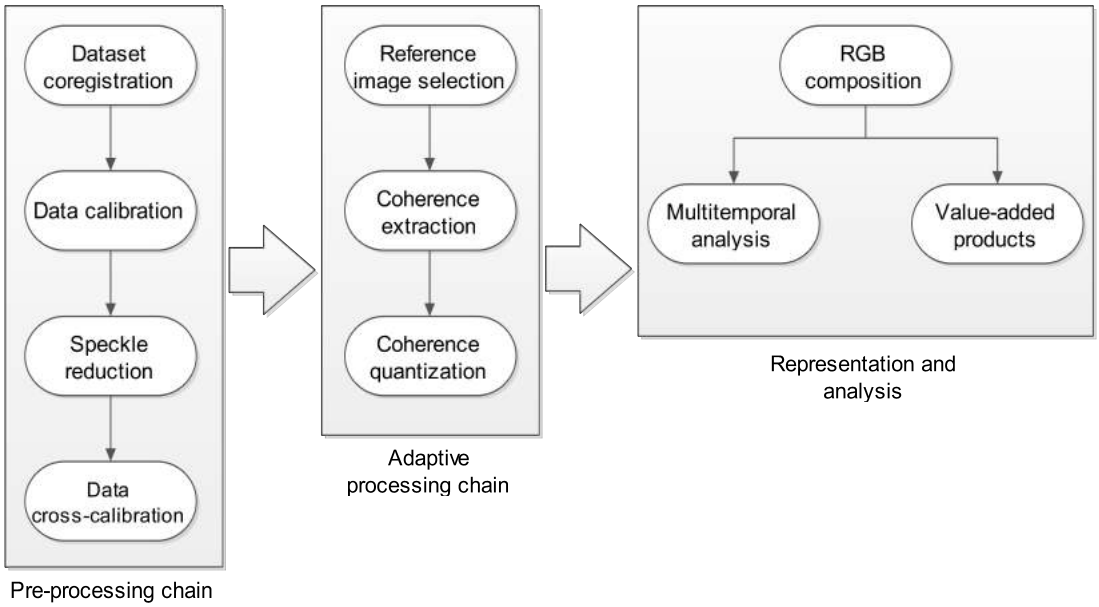

Fig. 2: Block diagram of the MAP3 framework.

The central block of the MAP3 framework should be application-adapted. We processed two datasets acquired by different sensors:

- The first dataset is composed by 15 stripmap COSMO-SkyMed balanced SLC images with 3 meters of spatial resolution acquired on the Yatenga region, in the North of Burkina Faso. This stack has been provided by the Italian Space Agency under the aegis of the project "Use of high resolution SAR data for water resource management in semi-arid regions" [37]. The application is oriented to water resource monitoring. The results of the application of MAP3 to this dataset are presented in Sections IV and VI in order to support the method presentation.
- The second dataset is composed by 35 stripmap TerraSAR-X SLC images with 3 meters of spatial resolution acquired on Ciró Marina, Calabria, Italy. This scene is characterized by a temperate climate and the application is oriented to agricultural monitoring. The results of the application of MAP3 to this dataset are presented in Section VII in order to stress the frameworks independence from both scene and sensor characteristics.

The COSMO-SkyMed stack allows us to stress some characteristics of our framework. It refers to a prevalently rural area (see Fig. 3) and includes a few small human settlements, mainly located close to water collection areas. Water harvesting is usually implemented via artificial dams created with (often) rudimental techniques along the course of streams. The major water reservoirs of Tougou, Ouahigouya, Gouinre and Lossa are, all over the year, clearly visually detectable both in optical (e.g., Google Earth), and SAR intensity maps. Moreover, there is a huge number of small basins (whose extension is in the order of a few thousand square meters) which are autonomously created by local population in order to satisfy their necessities in terms of water supply. These basins are crucial for human activities, but are often not censed nor surveyed, and cannot be easily monitored via available remote sensing techniques.

The strong variability of this scenario is evident in Fig. 4. In particular, in Fig. 4a and Fig. 4b two Google Earth views of the Tougou basin acquired on 2013, May 5 (Fig. 4a) and 2008, October 30 (Fig. 4b) are shown. The change in the response of the scene according to the season is evident. The same consideration can be made looking at Fig. 4c, and Fig. 4d where two small reservoirs located in the nearby of the Aoréama settlement are shown. In this case, the water surfaces are visible only in the acquisition of October (Fig. 4d), while in May (Fig. 4c), at the end of the dry season, the water intakes are empty. The introduction of the multitemporal Level 1α products arose from the necessity of monitoring the dynamics of these quickly variable phenomena. The required processing blocks, shown in Fig. 2, are analyzed and discussed in detail in the following sections.

IV. Pre-processing chain

A. Coregistration and speckle reduction

Data coregistration and speckle reduction are the first two steps of the processing chain, as shown in Fig. 2. Data must be spatially registered with sub-pixel precision (typically 1/8 or better), as required by the evaluation of the interferometric coherence.

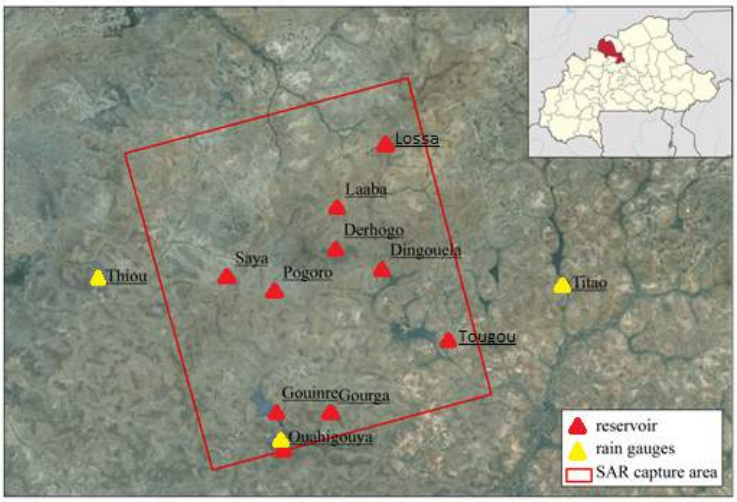

Fig. 3: Google Earth view of the Yatenga region, Burkina Faso, acquired on 2008, October 30. The red rectangle, representing the data-take, covers an area of approximately 1600 km^2.

(a) (b)

(c) (d)

Fig. 4: Google Earth views of the semi-arid dataset acquired on (a), (c) 2013, May 5 and (b), (d) 2008, October 30.

A typical SAR registration procedure involves three steps. The first step is a coarse alignment performed with the aid of satellite orbit data which are used to solve the Range-Doppler equations coupled with an Earth ellipsoid model. This produces an alignment in the order of few pixel.

The second step is a procedure based on the evaluation of the cross-correlation between a series of windows uniformly distributed over the two processed images [38]. The position of the peak of the cross-correlation matrix identifies the shift to be applied to the slave image window in order to obtain the maximum similarity with the homologous masters one.

In case of complex data, a further step can be performed computing the interferometric coherence between a series of uniformly distributed small windows. This is a two-dimensional optimization problem which is usually solved with Powells method since it requires no information about the derivatives of the function to be minimized [39].

Finally, the coregistration function can be provided as a smooth polynomial that approximates the pixel-to-pixel shift with the assumption of targets lying on the ellipsoidal Earth surface [40].

In multitemporal analysis, a despeckling phase of the available dataset assumes a key importance, since the detrimental effects of speckle presence could significantly alter the discrimination of the features along the temporal axis [41].

The availability of a multitemporal set of SAR images offers the opportunity to develop filters that preserve the original spatial resolution [42]. Several studies have been proposed on this issue [43]–[47]. In this work, the speckle reduction is performed by employing the optimal weighting multitemporal De Grandi filtering [44] because of its availability on commercial software and excellent declared performance in terms of Equivalent Number of Looks (ENL) on simulated SAR data. An example of the effects of the filtering process is shown in Fig. 5, where we compare the SAR image of the Laaba dam before and after the filtering procedure. In Fig. 5b we can observe that the significant reduction of the speckle, which is in the order of 12 looks with no loss in spatial resolution, did not deteriorate the spatial boundaries. In addition, the contrast between the open water and the surrounding environment is increased.

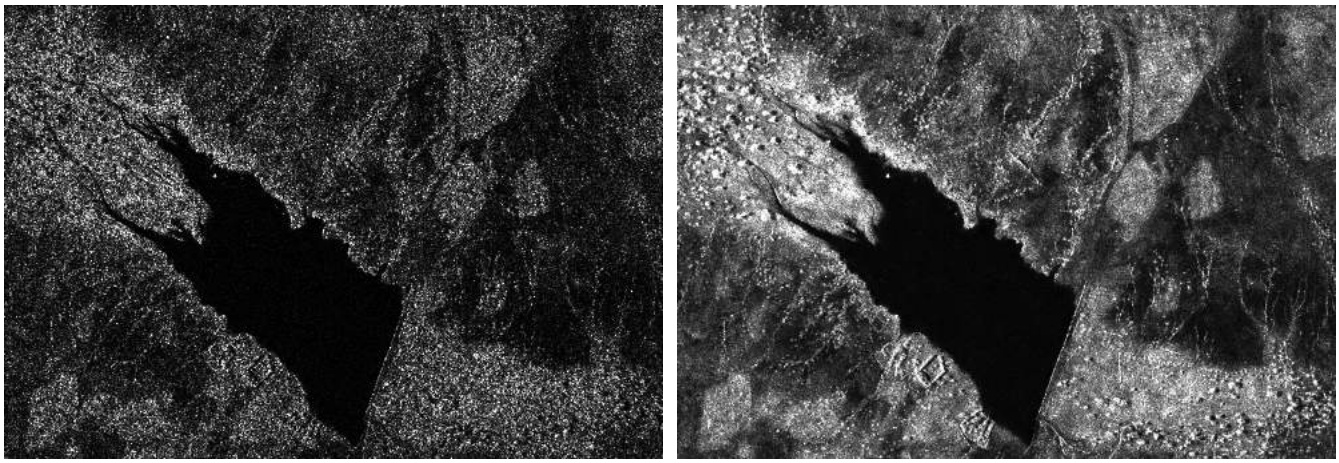

(a) (b)

Fig. 5: Laaba basin, 2011, October 09, intensity map before (a) and after (b) the application of De Grandi multitemporal filter.

B. Data calibration

One of the major challenges of the processing chain is to create a series of radiometrically comparable images. As explained in [48], COSMO-SkyMed Single Look Complex Balanced products (described in [31]) are corrected from the effects related to the sensor and the acquisition geometry. The sigma naught can be evaluated applying a calibration factor calculated from ancillary data. The list of the available product dates and the corresponding calibration factors is presented in the first two columns of TABLE I. Note that these coefficients refer to the SLC data, hence they should be applied to the power image before the filtering step.

If the provided calibration coefficients are found to be not satisfactory, a further calibration can be performed using an image-based technique. In fact, the calibration accuracy of a time series with N_I images can be improved using a Permanent Scatterer (PS)-based technique such as PSCal proposed in [35]. The goal of this technique is to identify the largest number of stable targets in the images and, through the evaluation of their response, retrieve the set of N_{I-1} differential gains with respect to unity. The PSCal technique turned out to be effective in many applicative contexts and its main limitations are explained in [49]. In this work, under the hypothesis that the PSs phases are unknown, we perform a non-coherent gain estimation, maximizing the log likelihood of the complex observations. This nonlinear maximization problem is then solved with the iterative method presented in [35].

In order to identify a reasonable set of PSs, we propose a method based on the fact that, if a target exhibits high coherence through the entire time series, it is a candidate to be classified as a PS. With a threshold value of 0.5, 5042 candidate PSs are selected. This population is tested in order to find the point targets that actually behave as PSs. The solution can be initialized assuming for the gains the $[1 \times N_I]$ unit vector $a^0 = [1, 1, \dots 1]$, where the apex indicates the iteration counter.

The set of gains found at the iteration $j-1$ is used to retrieve the PS amplitudes and noise variances. The detection is performed applying a threshold of 0.8 on the Generalized Likelihood Ratio Test (GLRT) [35] which leads to 4059 PS found after 118 iterations with a convergence criterion $a^j - a^{j-1} < 10^{-6}$.

Fig. 6 shows a De Grandi-filtered intensity map for the Tougou basin site with the PSs positions in red. As expected, in this rural area, PSs are found in correspondence with the small human settlements.

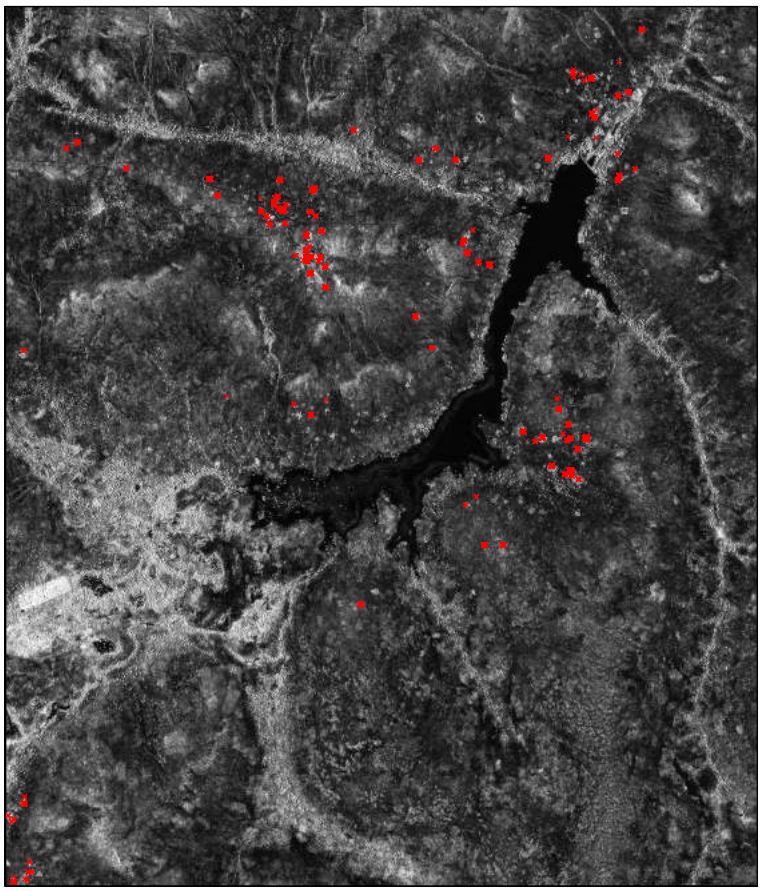

Fig. 6: Tougou basin: PSs positions.

The third column of TABLE I shows the PSCal calibration coefficients with respect to the reference image, (2011, April 28). This result is congruent with COSMO-SkyMed products specifications, according to which the calibration accuracy is smaller than 1 dB [31], [32].

TABLE I: Internal calibration coefficients (second column) and PSCal estimated coefficients (third column) in dB. All the images are acquired with HH polarization, ascending orbit and look angle of $\approx 33°$.

Acquisition date	Internal calibration	After PSCal
2010-06-12	-54.6908	-0.124
2010-06-13	-55.5859	-0.643
2010-07-14	-55.7245	-0.249
2010-08-15	-53.8149	0.899
2010-08-31	-54.3616	0.340
2010-09-16	-54.8973	0.220
2010-12-05	-56.0023	-0.192
2011-03-27	-55.3059	0.014
2011-04-28	-55.7180	1.000
2011-04-29	-55.8170	-0.349
2011-07-17	-55.2849	0.533
2011-08-02	-53.9722	-0.052
2011-10-09	-54.0330	-0.070
2011-11-10	-55.2586	-0.089
2011-12-12	-54.7326	-0.094

C. The VALE method

In order to combine the images of the time series in a color composite view it is necessary that data are expressed in a common scale with a number of levels (usually 256) suitable with human visual perception. In [25] this problem has been solved for flood monitoring by studying the confidence intervals using percentiles, and applying a histogram clipping in correspondence with the percentile that best preserves the image entropy, followed by a 256 levels rescaling and equalization.

The above cited method requires that "only marginal changes (statistically speaking) have occurred from one date to the next" [25]. This is not the case in many applications, mainly if agricultural cycles are under observation. In addition, equalization is a nonlinear and image-dependent process, which alters the intensity ratios between the images, especially where histograms slopes are higher. In semi-arid regions, the distribution of the information (i.e. the shape of the histogram) is strongly variable between the dry and the wet season due to the variability of surface water and vegetation cover. As a consequence, the histogram clipping, although guided by the best entropy preservation criteria, could cause the association of the same amplitude level to different bins during the byte scale operation. This would bring to errors in the evaluation of the time series.

These considerations suggest that a reliable criterion of comparability between a series of images must be the conservation of the amplitude ratios. The processing must guarantee that the same reflectivity values are represented in the same histogram bin for all the images of the time series.

Assuming that data are perfectly calibrated, it is possible to establish a metric for the entire time series selecting a common threshold for the clipping of all the histograms. This allows the preservation of the amplitude ratios between the images. For this purpose, we propose the following processing chain, which establishes the VALE method:

1. Let N_I be the number of images belonging to the time series and $M_i, i \in [1, 2, \ldots, N_I]$ the maximum amplitude value of the $i-th$ image; the vector $\mathbf{M} = [M_1, M_2, \ldots, M_{N_I}]$ is defined.
2. Let be p the position of the minimum in $\mathbf{M}$, i.e. $M_p = \min\{\mathbf{M}\}$. The $p-th$ element of the series is then the image with the minimal dynamics and is assumed as reference for establishing the amplitude threshold. This ensures that the threshold value exists in all the images of the series;
3. All the histograms of the series are clipped at an amplitude value $\hat{A} = qM_p$, with $q < 1$ evaluated on the $p-th$ image. This ensures the best compromise between the entropy preservation and the minimization of the percentage of saturated pixels. The optimum percentile is established based on considerations on SAR image probability density function.
   As known, single look SAR images pdfs are strongly asymmetric and characterized by a very long right tail. Hence, the skewness parameter exhibits positive values much greater than zero. This means that most of the information is grouped in a limited percentile of the cumulative histogram. The image entropy can guide in the search of this percentile. In fact, as reported in [25], when q tends to unit, the entropy has an abrupt fall, i.e. a large number of amplitude values are compressed in a few histogram bins. Our experiments, whose results are reported in TABLE II, reveal that the best clipping value is found to be the 98% of the cumulative histogram, hence for $q = 0.98$. In fact, although the maximum entropy is reached at a lower percentile, the choice of the 98^{th} percentile allows us to saturate a minor percentage of pixels with negligible loss in entropy. In this case, entropy can be a reliable guide in order to select the best clipping value since we are considering a single image, for which the best preservation of the informative content is desirable.
4. All the histograms will be clipped at the same amplitude value qM_p, corresponding to the same binsize value $\hat{b} = qM_p/255$. In this way the metrics of the time series is established.

TABLE II: Images entropy as a function of the clipping percentile. In chain A all the histograms of the time series have been clipped at the same percentile. For chain B the percentile value refers only to the reference image of the series. Image T2 refers to March 2011, while image T1 to August 2010.

	A		B	
Percentile	T1	T2	T1	T2
90^{th}	7.544	7.454	7.425	6.103
91^{th}	7.580	7.458	7.460	6.286
92^{th}	7.603	7.489	7.485	6.454
93^{th}	7.615	7.508	7.502	6.606
94^{th}	7.620	7.515	7.511	6.743
95^{th}	7.617	7.511	7.507	7.076
96^{th}	7.582	7.499	7.498	7.163
97^{th}	7.544	7.459	7.452	7.364
98^{th}	7.343	7.270	7.320	7.571
99^{th}	2.840	2.398	2.842	3.634
100^{th}	$9.8E^{-4}$	$1E^{-3}$	$1.3E^{-3}$	$1.5E^{-3}$

To illustrate the validity of these claims, let consider the two SAR images depicted in Fig. 7, representing the neighborhood of a dam in two extreme conditions. In fact, Fig. 7a and Fig. 7b were acquired on August 2010 at the peak of the wet season

and on March 2011 at the end of the dry season, respectively. The red rectangle (subset A) is relative to an area in which the vegetation is homogeneous and persistent all over the year; the green rectangle (subset B), instead, is a surface-water zone. Hence, both the subsets are relative to a homogeneous area in which the electromagnetic response is expected to be almost stable, despite of the strong variability of the surrounding scene. The effects on the amplitude ratios of the cross-calibration based on the percentile approach with respect to VALE are evaluated by selecting ten sample subsets of type A and of type B, randomly distributed on the two scenes. They have been processed with the following methods:

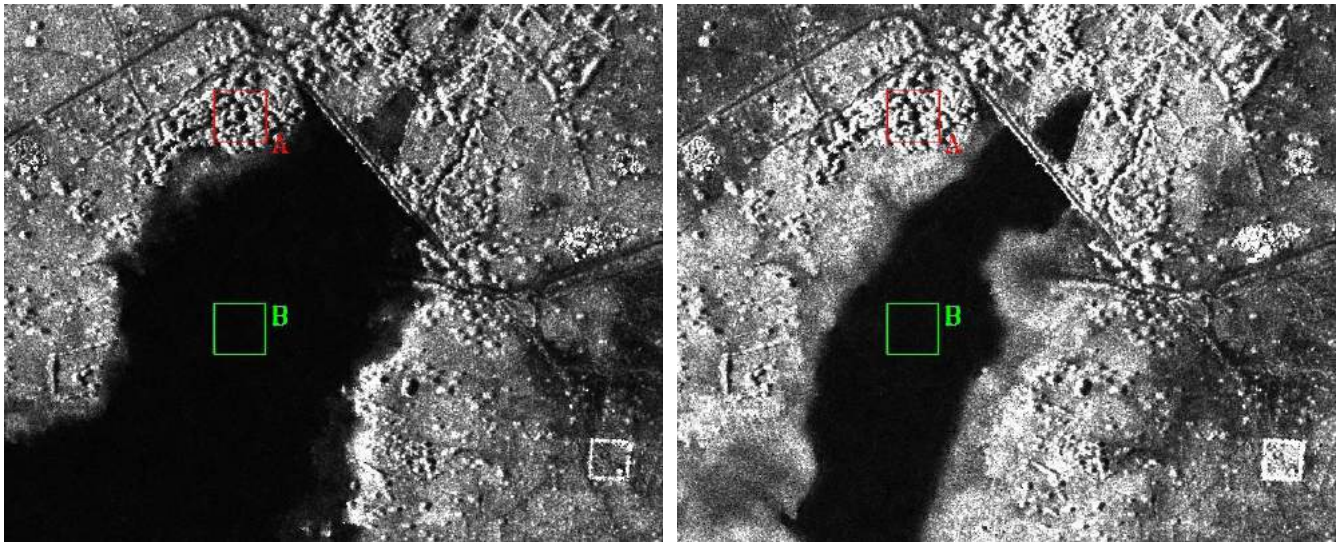

(a) (b)

Fig. 7: Particular of the Tougou dam for the acquisition of 2010-08-31 (a) and of 2011-03-27 (b). The red rectangle (subset A) is relative to a homogeneously and persistently vegetated area; the green rectangle (subset B) is taken in a surface-water area.

- Chain A: percentile-based clipping and rescaling between $[0, 255]$, as proposed in [25]. The histograms have been clipped at the same percentile of the cumulative histogram, thus resulting in a non-uniform binsize in the rescaling procedure.
- Chain B: the proposed cross-calibration method (VALE). VALE calls for: calibration through the application of the coefficients reported in TABLE I, amplitude threshold-based clipping and rescaling between $[0, 255]$. The histograms are clipped at the same intensity value; hence, the corresponding percentile in the cumulative histogram should be different, but the binsize in the rescaling procedure is the same for all the images.

Fig. 8 shows the scatterplot (mean vs. standard deviation) for the above introduced images processed with chains A and B. We have indicated with T1 and T2 the acquisitions of August 2010 and March 2011, respectively. Fig. 8 reveals that the two cross-calibration methods bring to conflicting results. As a matter of fact, the class vegetation for the T1 image (August, wet season) is placed to the left of the class vegetation for the T2 image (March, dry season) in the case of chain A processing and to the right in the case of chain B processing. The physically consistent result is obtained with the proposed method, since we expect a higher electromagnetic response during the wet season thanks to the enhancement of the volumetric backscattering due to the growth of the leafs. Surface-water areas, unlike vegetated ones, are only slightly affected by the choice of the clipping method. Therefore, for flooding applications, as in [25], both the chains are almost equally suitable.

However, our method makes possible a better separation between the classes because of the centers of mass of the population relative to the class water and vegetation are more distant in both the images if processed with VALE (i.e. chain B).

TABLE II reports the entropy analysis for the two test images. The entropy has been calculated with the following relation [50]:

$$H = \sum_{n=1}^{N} -P_n \log_2 P_n \tag{1}$$

where P_n is the normalized probability of the n-th quantization level of the histogram and N the total number of bins.

The analysis reported in TABLE II highlights that VALE ensures high values of entropy for the processed images. It arises that the images processed with the VALE method have an entropy value that is close to the theoretical limit (i.e. 8), which would be assumed by an uniform distribution. This confirms VALE robustness, since it preserves the amplitude ratios between the images and it ensures their informative content.

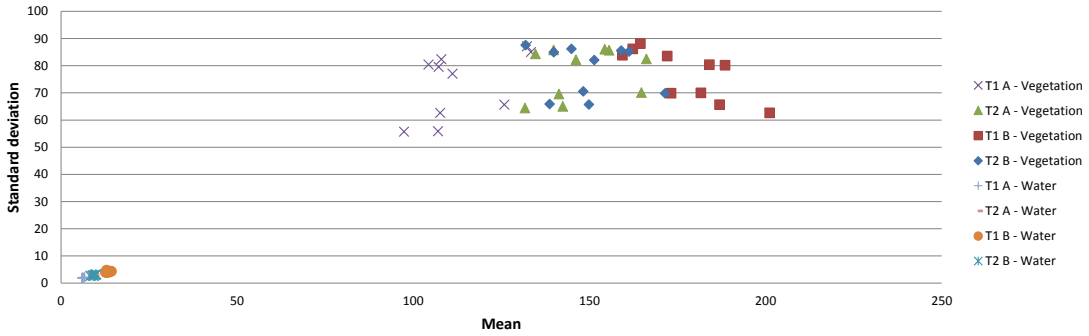

Fig. 8: Scatterplot of mean vs. standard deviation for ten sample subsets representing homogenous vegetated areas and surface-water areas, as in Fig. 7, processed with the chain A and the chain B (VALE).

V. Climate-adapted chain

The guideline for building the new multitemporal Level 1α products that is discussed in this section consits in exploiting *a priori* information on the climatic variability typical of semi-arid regions, which are characterized by a long dry season (from October to May) and an intense wet season (from June to September). The activities embodied in the Adaptive Processing block (see Fig. 2) are tailored on the particular available dataset.

In Fig. 9 the average of monthly rainfall for the three stations marked in Fig.1 1 is reported. About 75% of the rain falls during the months of July, August, and September, while from November to April rainfall is lower than 20 mm par month [51]. The response of the scene to the rain forcing depends on the terrain:

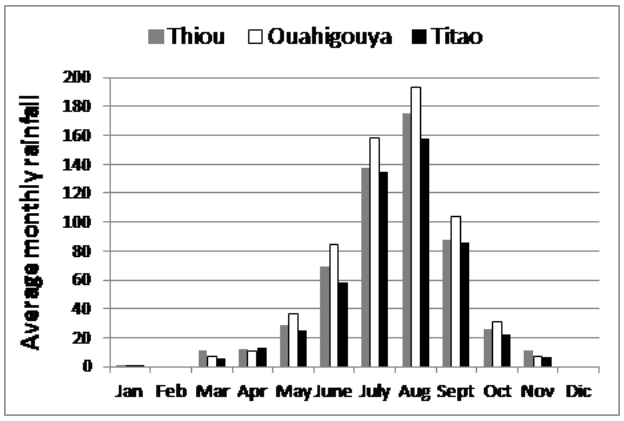

Fig. 9: Average monthly rainfall computed over the period 1974-2011.

- Cultivated areas experience a growth of vegetation correlated with the rain trend. The same behavior holds for uncultivated areas that are not eroded; at the end of the dry season, most of the terrains are almost completely bare.
- Eroded areas have lost the capability of absorbing water, so that their dielectric characteristics are stable during all the year;
- Reservoirs fill up rapidly during the wet season and empty almost completely during the dry season. This happens especially for small dams located in rural areas.

The electromagnetic reflectivity of the scene depends on these phenomena. As a matter of fact, a high electromagnetic response is expected on vegetated areas because of an enhancement of backscattering due to volumetric effects and plant-land interaction [52], [53]. Vice versa, a low response is expected on bare soils and ponds.

A. Interferometric coherence extraction and quantization

As known, the interferometric coherence is given by the relation:

$$\gamma = \left| \frac{E\left[I_1 I_2^*\right]}{\sqrt{E\left[\left|I_1\right|^2\right] E\left[\left|I_2\right|^2\right]}} \right| \tag{2}$$

where the operator $E[\cdot]$ denotes statistical expectation and the apex $*$ the conjugate operation. This quantity is an indicator of the phase stability of a target. Hence, dealing with multitemporal series in which the images could have very large temporal baselines, we expect high values for γ only in correspondence with fixed man-made structures. In other words, when a long term interferometric coherence is computed, the result is an almost binary mask composed by "coherent" and "not coherent" points. Therefore, we impose that points whose interferometric coherence is below an assigned threshold are classified as "not coherent" and placed in the first histogram bin during the rescaling operation. For prevalently rural areas, a reasonable threshold value turns out to be 0.45.

VI. Multitemporal Level 1α products

The pre-processing blocks described in Section IV guarantee the comparability of amplitude images. Therefore, according to the third block of Fig. 2, it is now possible to reproduce a multitemporal set of SAR images in order to improve the image interpretation and to facilitate the SAR image features extraction.

The key aspect for evidencing a desired feature is the identification of a reference scenario, characterized by the fact that the physical parameters to be retrieved present extreme values. In semi-arid regions, this reference situation occurs at the end of the dry season, usually in April, when terrains are almost completely bare and the ponds are empty. Therefore, it is possible to detect the features of interest by comparing an image acquired in a date under test (test image) with a reference image, acquired at the end of the dry season.

All the Level 1α products proposed in the following represent a subset of the scene depicted in Fig. 3 and cover an area of approximately 15 km $\times$ 18 km. The used combination of bands is the following:

- Red band: Coherence map;
- Green band: Test image;
- Blue band: Dry season image (2011, April 28).

Fig. 10 provides a synthetic instrument for the interpretation of the images. The coherence introduces the third dimension, with a high contribution of the red band for man-made structures which, as a consequence, will appear as bright targets on the maps.

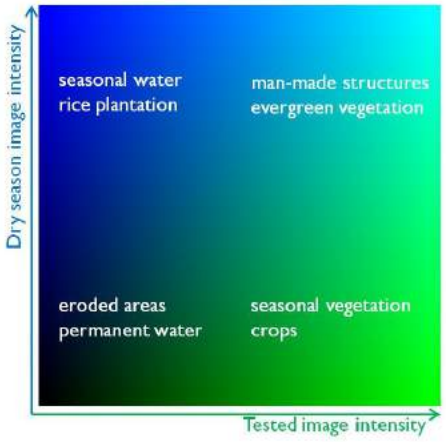

Fig. 10: Interpretative tool.

The band-color association has been chosen in order to help the image comprehension. In Fig. 11 and Fig. 12 the blue band is associated with the presence of water and the green band is related to the presence of vegetation. In particular, in Fig. 11 the test image was acquired in 2010, August 31, and was loaded on the green band. The growth of vegetation provokes an enhancement of the backscattering in August such that the green band amplitude will be dominant with respect to the red and blue bands. Areas covered by seasonal surface water appear in blue because in the wet season the ponds are filled up by intense rainfalls, the water acts as a reflector, and the corresponding backscattering (green band) is significantly weaker with respect to that of the reference dry situation (blue band). Permanent water appears as a black area within the basin, because of the low electromagnetic response both in the dry and in the wet season. The adjective "permanent" specifies that this feature is present on the scene all over the year.

The product depicted in Fig. 12 is obtained through a composition of two images belonging to the dry season. The test image (green band) is acquired on 2011, March 27. In this case, the cyan is the dominant color because the electromagnetic response of the two scenes is almost unchanged, except for the areas in which the counter-season agriculture is exercised, in the immediate neighborhood of the river streams. Therefore, those areas are characterized by green pixels. Similarly, blue color is related with seasonal water.

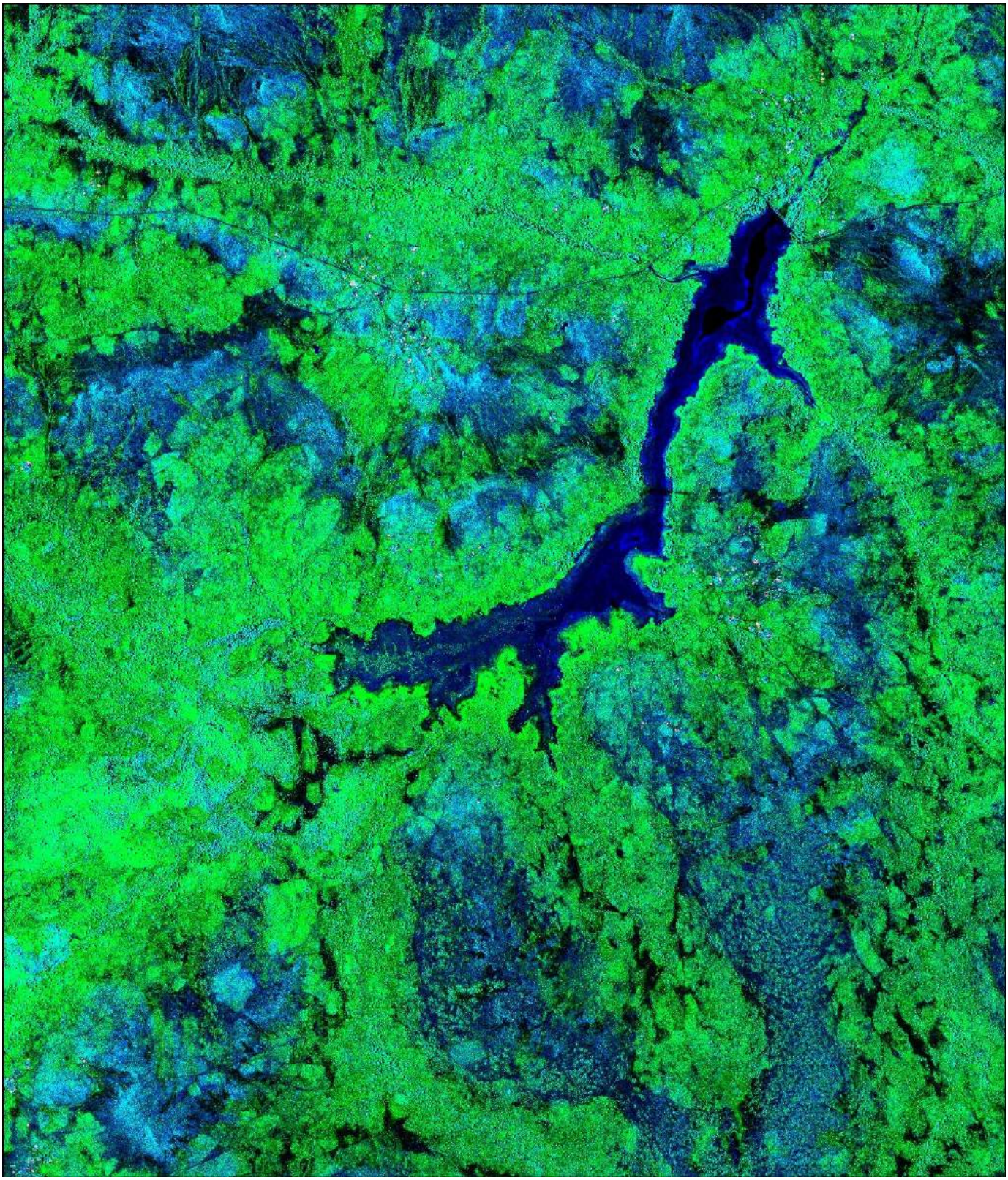

Fig. 11: Tougou basin, COSMO-SkyMed Level 1α product. Blue band: 2011, April 28 (dry season); Green band: 2010, August 31 (wet season); Red band: interferometric coherence.

In Fig. 13 the Level 1α products for the entire analyzed time series are shown. From this representation, which covers about one year and a half, the potentiality of the proposed products in the comprehension of the dynamics of the scene is emphasized. The cycles of the vegetation and of inland water can be quantitatively correlated to the rainfalls. In addition, the

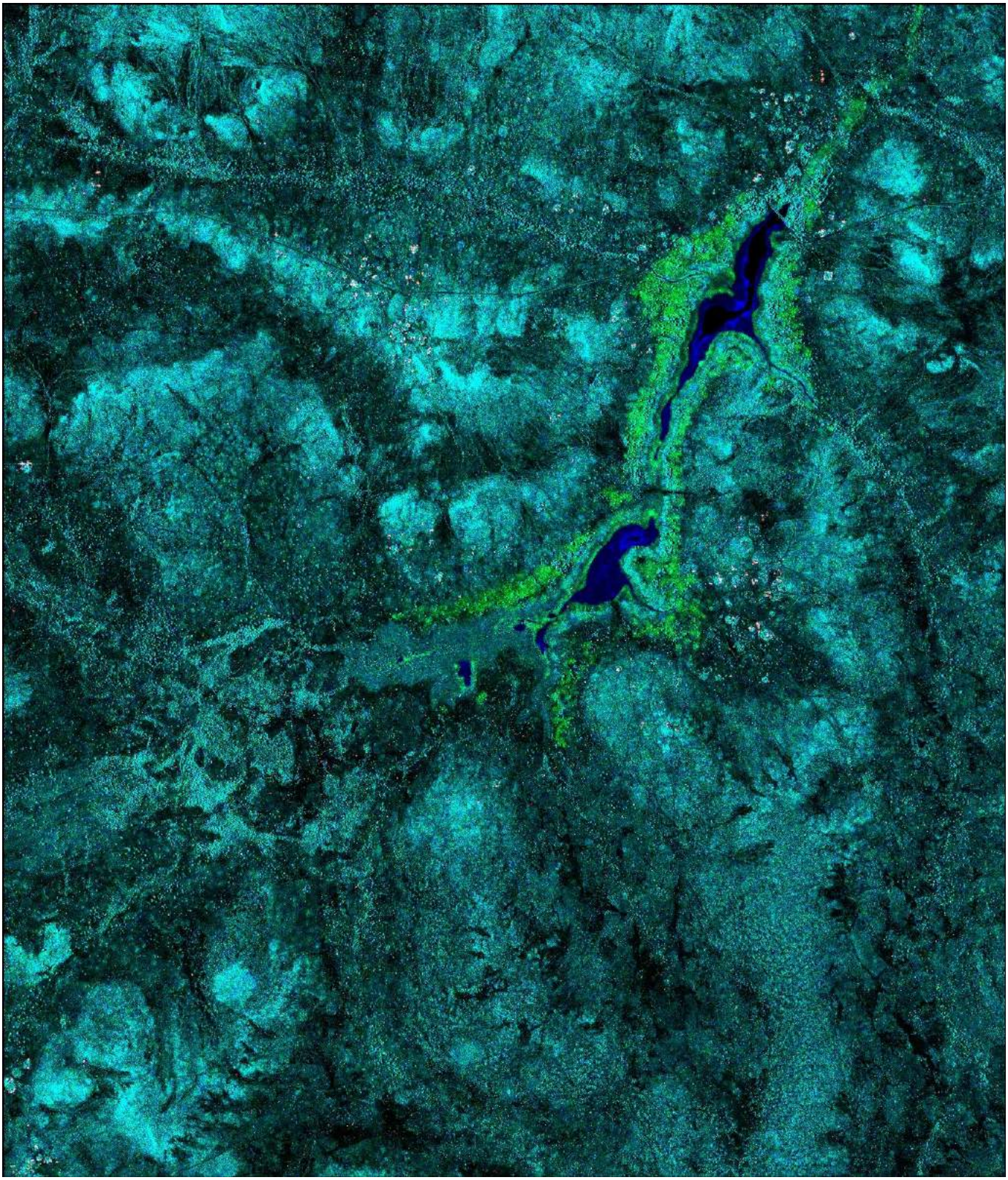

Fig. 12: Tougou basin, COSMO-SkyMed Level 1α product. Blue band: 2011, April 28 (dry season); Green band: 2011, March 27 (dry season); Red band: interferometric coherence.

increasing of vegetated surfaces during the wet season and the water amount in the intakes can be easily monitored.

Furthermore, in this context, the new products provide immediate information about the location of villages otherwise hardly locatable, as shown in Fig. 14a. As a matter of fact, human settlements appear as bright points because they are characterized

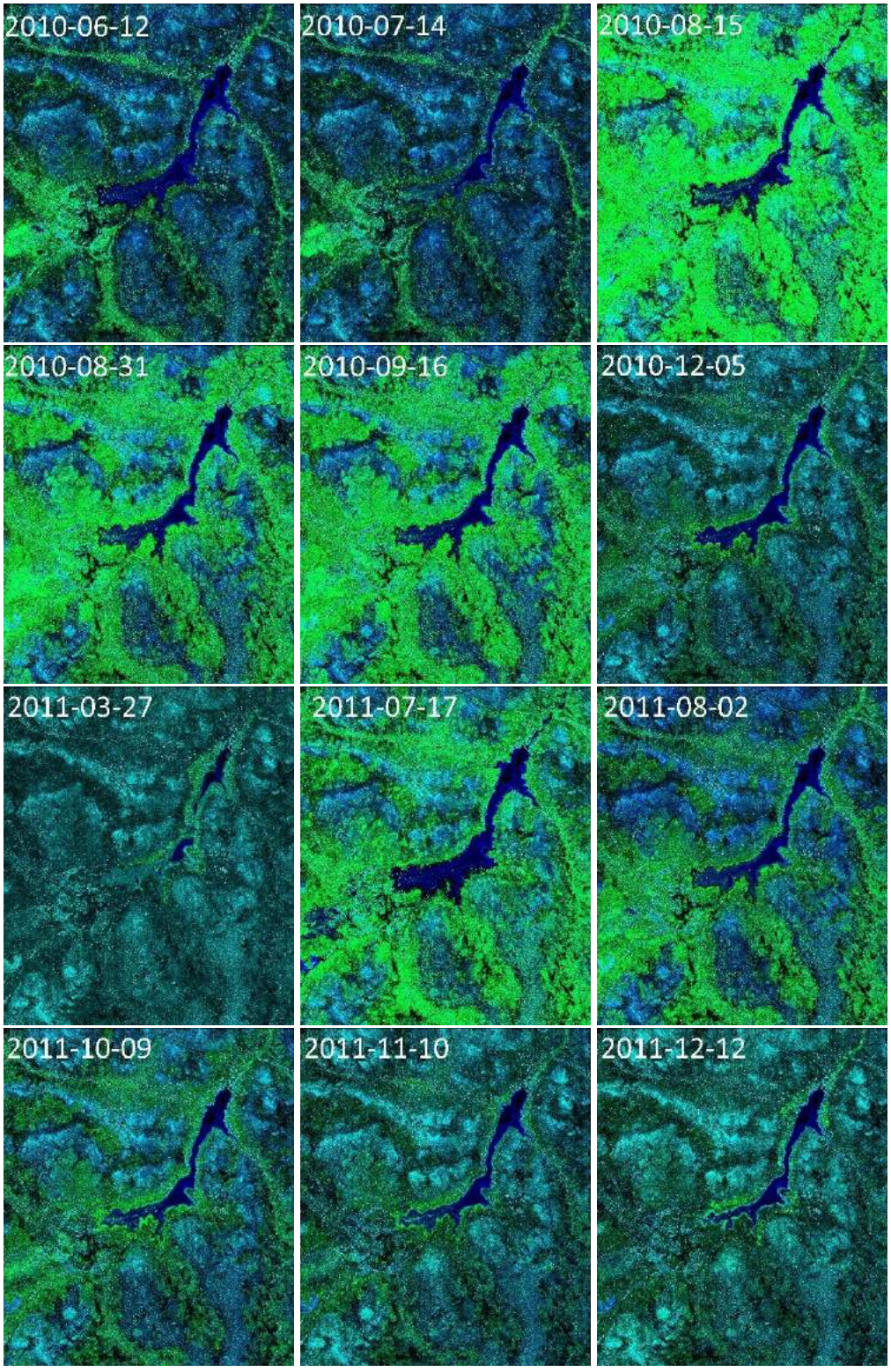

Fig. 13: Tougou basin, multitemporal series. Reference image (blue band): 2011/04/28 (dry season). Test images from left to right and up to down: 2010/06/12, 2010/07/14, 2010/08/15, 2010/08/31, 2010/09/16, 2010/12/05, 2011/03/27, 2011/07/17, 2011/08/02, 2011/10/09, 2011/11/10, 2011/12/12.

by high intensity of the electromagnetic response all over the year and high values of interferometric coherence, since they are stable in phase. However, it is worthwhile to note that in these areas even buildings can be not stable in phase since they are frequently made up of terrain and/or stones.

Note that the detection of human settlements can be evaluated by any couple of images, independently of the season, because a man-made structure has a stable reflectivity. Therefore, the Level 1α products introduce not-straightforward representations easy to interpret for humans and machines. In Fig. 14a and Fig. 14b it can be appreciated that trees appear in cyan, since their response is not coherent but stable in amplitude, and man-made structures appear in white, since their response is stable in both amplitude and phase. In general, the new products allow a simpler separation (even at visual level) between natural targets and man-made targets with respect to traditional SAR intensity maps.

In synthesis, the key aspect of the new products is the emphasis on the dynamics of the phenomena and their cyclic nature. The great advantage introduced by the proposed products is the immediacy of the information and the possibility to evaluate qualitatively the evolution in time of the features of interest.

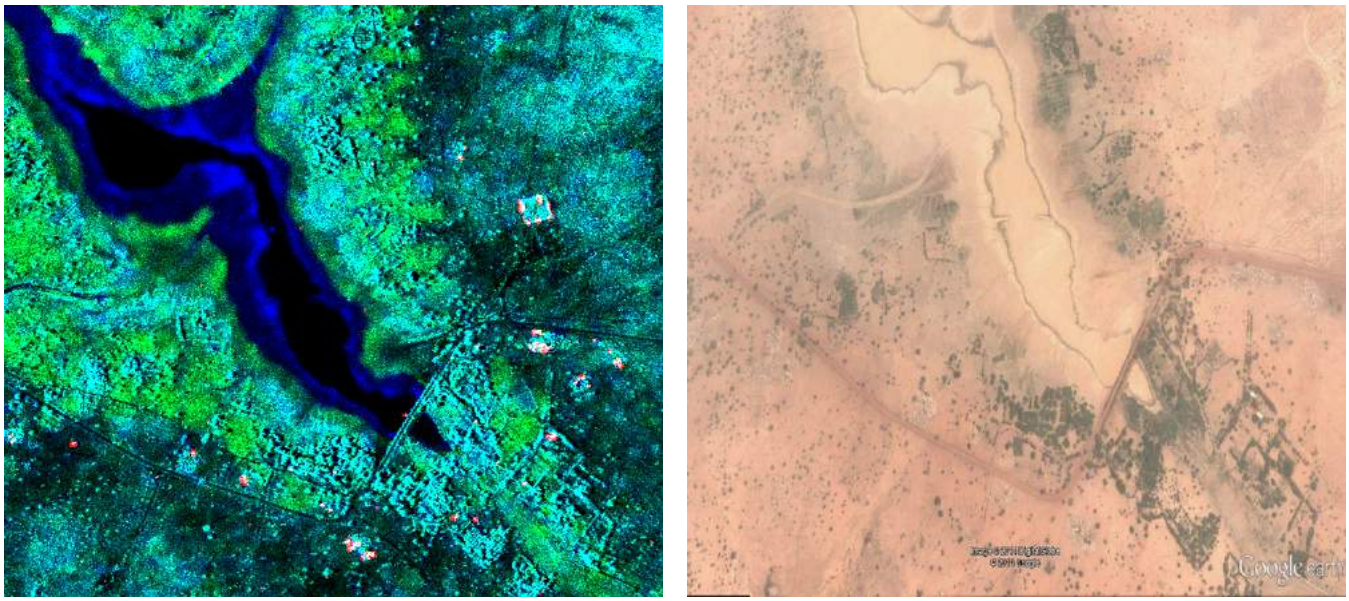

(a) (b)

Fig. 14: Tougou basin, particular of the Level 1α product (a) and Google Earth view (b).

In order to better appreciate the quality of the proposed products, we show in Fig. 15 (test image 2010, August 31) a close-up which allows to highlight the level of detail achieved. As a matter of fact, in Fig. 15a the dam, the road crossing it as well as the trees are clearly distinguishable. In Fig. 15c, instead, the presence of a small settlement and of a rudimental agricultural infrastructure in the upper right corner of the image is evident. It is also evident the enhancement provided with respect to the SLC products of the same area (acquired on 2010, August 31) depicted in Fig. 15b and Fig. 15d.

VII. Application of MAP3 in Temperate Zone

In order to test the generality of the proposed framework from both the sensor and the scene standpoint we processed a stack of 35 TerraSAR-X images (for calibration issues on this sensor see [54]) acquired on Ciró Marina, Calabria, Italy, an area characterized by a temperate climate. The results presented below have been obtained with the same parameters (i.e. histogram clipping parameter, interferometric coherence threshold, band combination and their disposition) adopted for the previous scene. Of course, the selection of the reference situation is guided by different criteria, depending on the phenomena to be monitored. The solution presented in Fig. 16 has been built taking as reference image the acquisition of 2010, January 1 (blue band) and as test image the acquisition of 2008, April 25 (green band). In this representation, the behavior of the relevant feature of the scene is the same of that previously analyzed for the Tougou basin. In particular:

- Permanent water surfaces (e.g. the sea) appear as dark areas because of the low response of all the involved channels;
- Urban areas are represented as bright areas due to the high contributions of both intensity and interferometric coherence channels;
- Cultivated areas exhibit a color that depends on the state of the terrain in the two dates and on the type of cultivation. Because of the high degree of anthropization, in this case the agronomic/botanic interpretation is not straightforward and needs to be supported by specific expertise.

The representation depicted in Fig. 17 is an exploded view of the bands composing Fig. 16. In particular, Fig. 17a and Fig. 17c represent the blue band and the green band, respectively. Fig. 17b shows the interferometric coherence calculated applying (2), while Fig. 17d depicts its quantized version. The reader should note how the shift of the first histogram bin

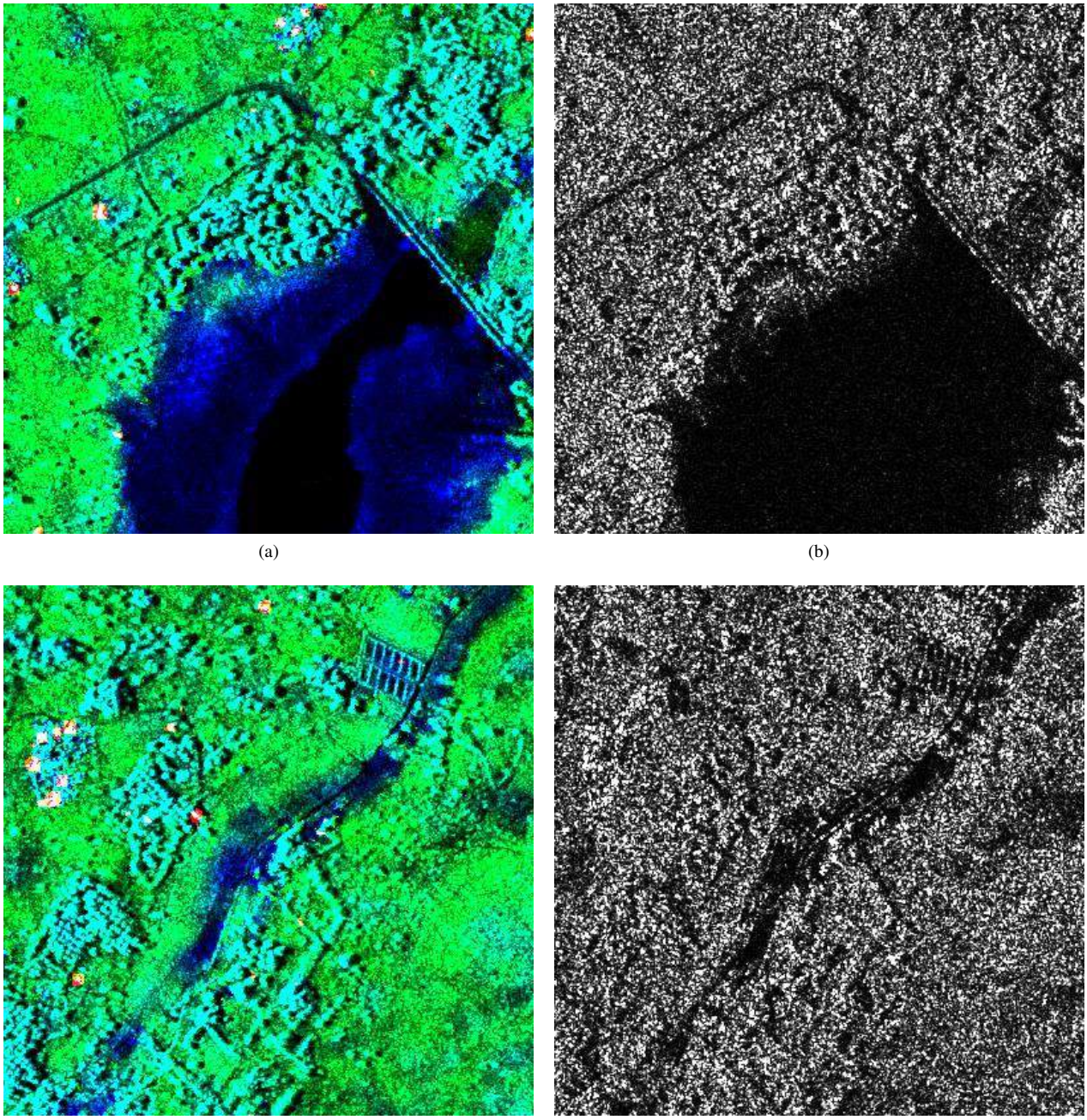

(a) (b)

(c) (d)

Fig. 15: Tougou basin, close up 400 $\times$ 400 pixels. Level 1α product (test image 2010, August 31) (a), (c) and SLC product (b), (d). The covered area is approximately 1.5 km^2.

value to 0.45 emphasizes the presence of urban areas and man-made structures, which appear as bright points on the dark background of natural surfaces, which are typically not stable in phase.

It is worthwhile to note that in highly urbanized areas, buildings are not the only coherent targets, as shown in Fig. 18, in which a comparison between the geocoded Level 1α product of Fig. 16 and a Google Earth view is depicted. Indeed, buildings are among the detected coherent targets (see Fig. 18a and Fig. 18d). In fact, guardrails and street lamps also appear as bright targets, as shown in Fig. 18b and Fig. 18e. Moreover, azimuth ambiguities present a coherent behavior since they are the replicas of stable targets [**?**]. Spurious coherent points can be detected, as well as rocks. However, these objects appear in red (see Fig. 18c) and thus they can not be confused with man-made structures, which, in turn, appear in white. This phenomenon can be mitigated considering an appropriate tuning of the quantization parameter, i.e. rising the lower bound in the quantization process, or considering the mean coherence of the entire time series.

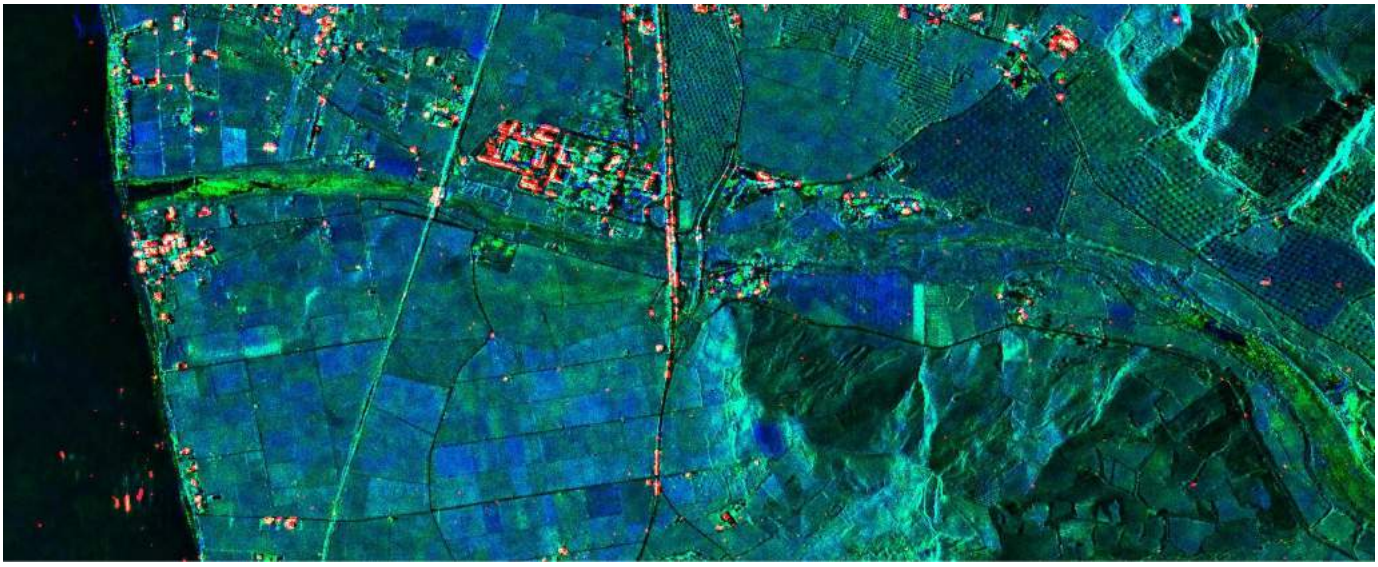

Fig. 16: Ciró Marina, TerraSAR-X Level 1α product. The imaged area is approximately 3 $\times$ 7 km^2.

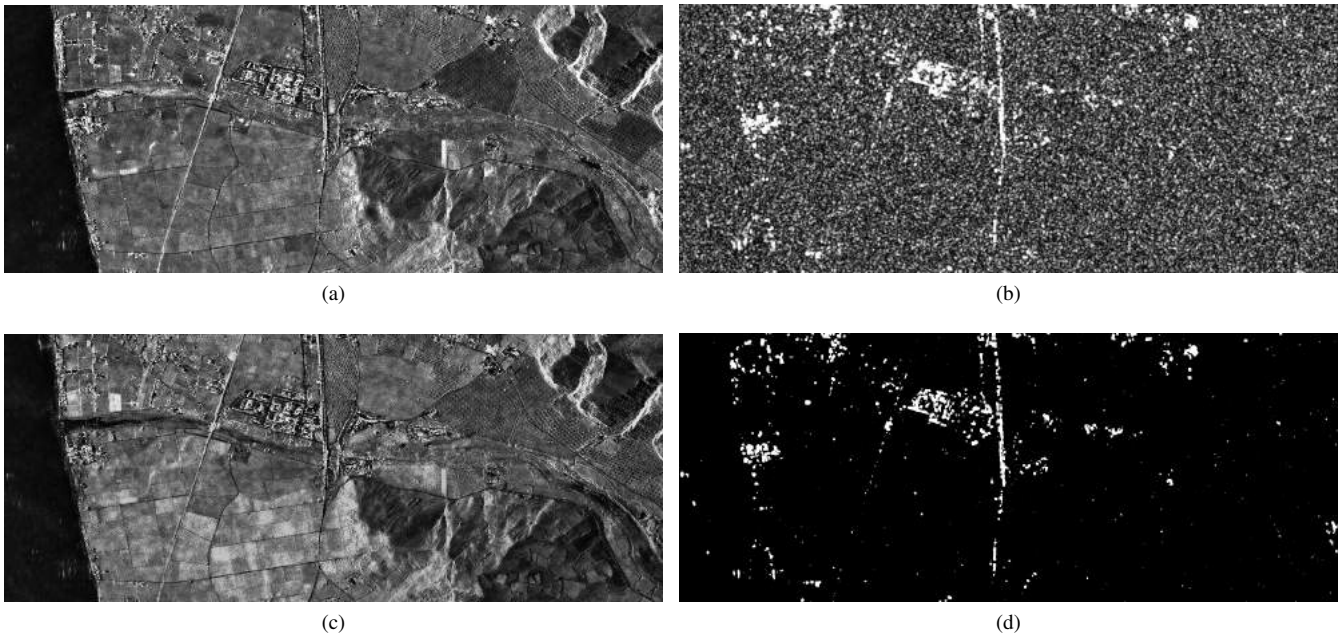

(a) (b)

(c) (d)

Fig. 17: Ciró Marina, Calabria, Italy. January amplitude map (a), April amplitude map (c), coherence map before (b) and after (d) the quantization procedure. The value of the first histogram bin has been set to 0.45.

In Fig. 19, the reader should appreciate the detail achieved by the proposed representation. In particular, in Fig. 19a a close-up of an alley cropping is reported. In Fig. 19b a small river is displayed. Note that the river was dry in April (green band), and water-filled in January (blue band). Therefore, the presence of surface water during the acquisition of January caused a weak blue-band amplitude in the area delimited by the river. The intensity of the green component witnesses the presence of vegetation or bare soil within the riverbed.

In synthesis, the change of sensor and scenario did not change the overall performances of the method.

VIII. Conclusions and discussions

Multitemporal SAR analysis is a powerful and attractive technique for environmental monitoring and planning. It introduces challenging issues relative to data calibration and their representation. This technique has been widely explored in the past (as discussed in Section II) but never coded in all its aspects. In this paper, we formalized the problem introducing the MAP3 framework, which, mixing state-of-art techniques and a novel cross-calibration method (VALE), brings to the extraction of a

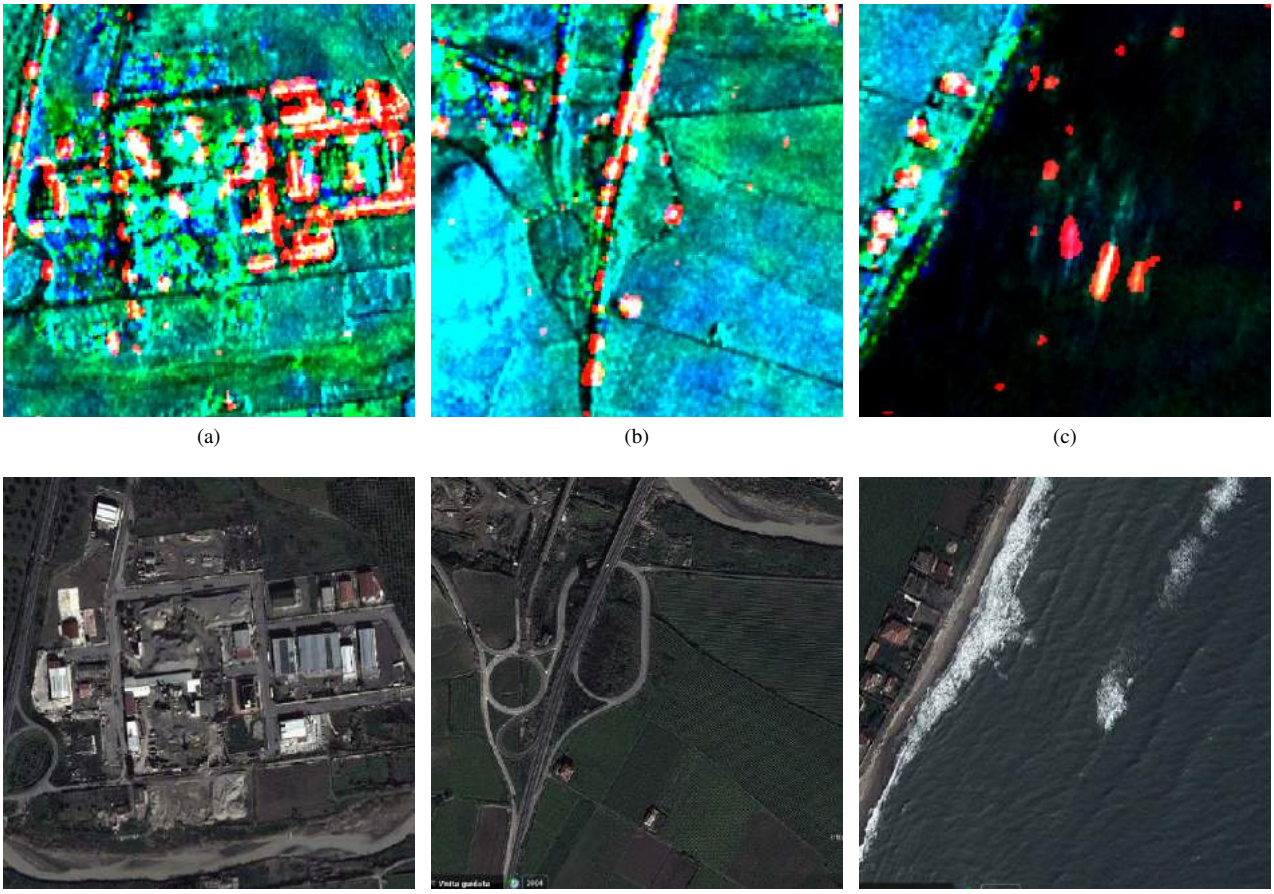

(a) (b) (c)

(d) (e) (f)

Fig. 18: Coherent targets in highly urbanized areas: buildings (a), (d), guardrails (b), (e) and azimuth ambiguities (c), (f).

new family of multitemporal products, the Level 1α products. These products are characterized by a context-adaptive nature, unlike the already available and generalist Level 1 products.

The MAP3 framework has been designed pointing to the minimization of the complexity and to the exploitation of the available algorithms. Innovation has been necessary in the cross-calibration phase, where we introduced the VALE method.

The proposed framework faced the challenges introduced in Section II the following solutions:

- Reproducibility: a well-defined and transparent framework for the elaboration of the proposed Level 1α products has been presented;
- Automation: the processing chain is highly automated with only a few parameters to set up, i.e. the coherence quantization threshold and the clipping percentile of the reference image histogram. The first is set based on the characteristics of the scene. In particular, for prevalently rural areas, a threshold of 0.45 is a reasonable zero-th quantization level. The second should be determined through an entropy analysis of the reference image;
- Adaptability: the processing chain can be adapted to different climatic zones and scenarios (see Section VI and VII);
- Reversibility: the proposed framework ensures the preservation of the electromagnetic information thanks to an accurate calibration of the channels involved in the processing. If the inversion of the channels is needed, it should be performed before any quantization;
- Visualization: we proposed to exploit the advantages derived from the RGB composition of suitable cross-calibrated channels in order to provide a comfortable and immediately interpretable experience of visualization of the maps;
- Interpretation: the proposed Level 1α multitemporal products bring a significant improvement in the SAR images comprehension and features identification applications.

Data calibration is the key aspect in multitemporal SAR data processing. As a matter of fact, the composition and the comparability of the elements of the series are possible only if the images are accurately radiometrically calibrated and, of course, spatially registered. In Section IV, we have shown how the internal calibration information provided by ancillary data can be refined and supported by external calibration techniques, as the PSCal method. We applied this refinement on our datasets in a few minutes using a machine with 12 GB RAM and an Intel Core i7 CPU 2.76 GHz clock. However, larger datasets could

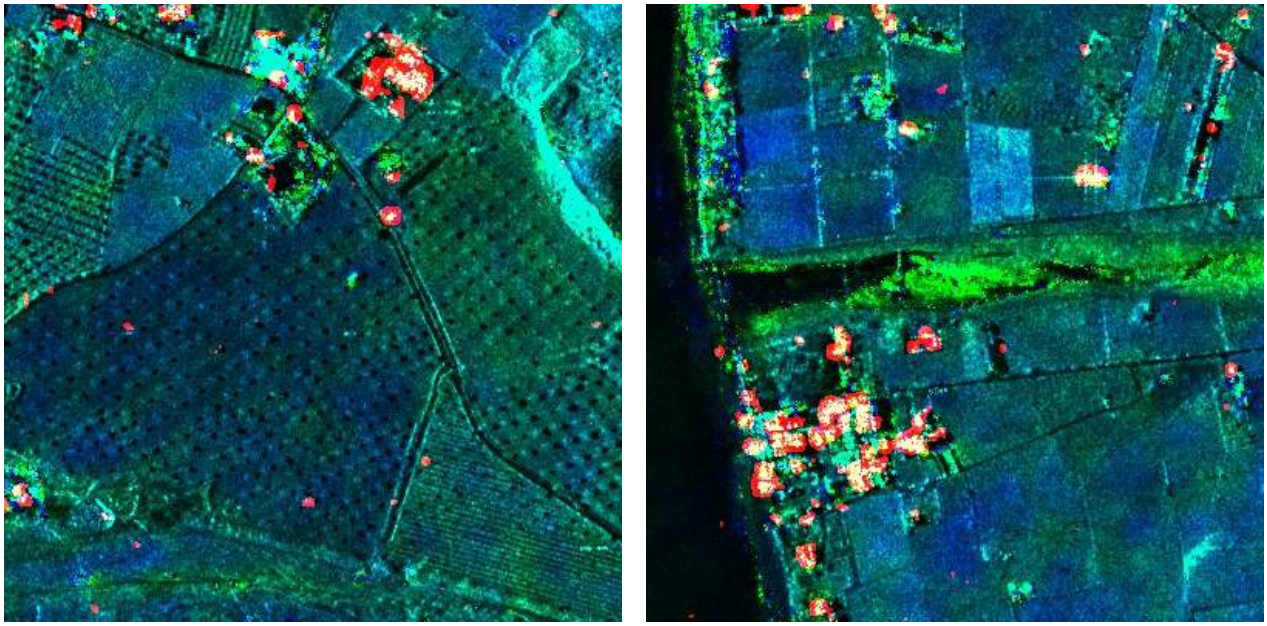

(a) (b)

Fig. 19: Ciró Marina, close up 400 $\times$ 400 pixels for a covered area of approximately 1.5 km^2. Alley cropping (a) and urban area near the seaside (b).

require a rather heavy computational burden. In this case, a trade-off based on the quality of the internal calibration should be considered.

The filtering step is fundamental for the reduction of speckle and for achieving a high quality final product. We have applied an optimal weighting multitemporal De Grandi filter achieving a speckle reduction equivalent to 12 number of looks, without losing spatial resolution.

The adaptive processing chain makes possible to model the proposed framework on the specific available dataset. We have experimented the method with images belonging to a semi-arid region, choosing a reference image at the peak of the dry season. This choice allowed us to identify the changes in vegetation cover and water availability. Moreover, the use of the interferometric coherence as the third band allows the identification of small human settlements, otherwise hardly detectable with classic SAR techniques. The same experiment has been performed in an area characterized by a temperate climate and the obtained results confirmed the effectiveness of the proposed framework.

The balance of the channels is ensured by the novel cross-calibration method that we called VALE. An image for each couple of the time series provides information about the evolution of the scene. The proposed products can be compared with thematic maps, even if at a lower level with respect to classification or land cover maps already available in literature, in the sense that Level 1α products shorten the distance between the so-called Level 1 and Level 2 products proposed by the providers of SAR data. In fact, our products can be easily managed by a large variety of users and are classification-ready, due to the clear separation between the classes present in the scene, either with simple unsupervised techniques or with a (minimal) interaction with the user. All these aspects, together with the interpretative immediacy given by the RGB composition, makes the proposed framework an attractive multidisciplinary tool for remote sensing based/aided applications. As a matter of fact, the relevant environmental phenomena, such as the growth of the vegetation and the change in the water availability determined by seasonal rainfalls, are clearly detectable and could be monitored. In this optic, the proposed framework could be a useful instrument for making previsions and for planning interventions on the scene.

The performed tests demonstrated that, under the hypothesis of perfectly calibrated data, the VALE processing chain ensures the preservation of the amplitude ratios between the images. This makes the VALE cross-calibration method superior with respect to the methods proposed in literature until now, since it allows the comparability of the histograms at low, intermediate and high intensity regions. This allows to push towards vegetation-oriented applications, up-to-now explored only with polarimetric data.

The proposed MAP3 framework is robust and flexible. In fact, on the one hand it can be replicated in different climatic zones and for different sensors, as shown in Section VII; in this case, the adaptive processing can be different but the results in terms of the enhancement of the semantic content of the images hold whatever the climate condition. On the other hand the techniques embodied in each block (for example filtering or calibration) can be substituted by others present in literature or implemented *ex novo*. Moreover, other blocks can be inserted in the processing chain in order to adapt MAP3 to the specific

application.

ACKNOWLEDGMENTS

The authors would sincerely thank Dr. Davide Notti from University of Pavia for providing the TerraSAR-X stack under the aegis of the project "Use of SAR-satellite data to monitor and model landslides and subsidence hazards".

REFERENCES

[1] H. B. Mitchell, *Image Fusion: Theories, Techniques and Applications*. Berling, Heidelberg: Springer-Verlag, 2010.
[2] J. M. Almendros Jimenez, L. Domene, and J. A. Piedra-Fernandez, "A Framework for Ocean Satellite Image Classification Based on Ontologies," *IEEE J. Sel. Topics Appl. Earth Observ.*, vol. 6, no. 2, pp. 1048–1063, 2013.
[3] V. Madhok and D. A. Landgrebe, "A Process Model for Remote Sensing Data Analysis," *IEEE Trans. Geosci. Remote Sens.*, vol. 40, no. 3, pp. 680–686, 2002.
[4] M. Datcu and K. Seidel, "Human-Centered Concepts for Exploration and Understanding of Earth Observation Images," *IEEE Trans. Geosci. Remote Sens.*, vol. 43, no. 3, pp. 52–59, 2005.
[5] J. T. Pulliainen, L. Kurvonen, and M. T. Hallikainen, "Multitemporal Behavior of L- and C- Band SAR Observations of Boreal Forests," *IEEE Trans. Geosci. Remote Sens.*, vol. 37, no. 2, pp. 927–937, 1999.
[6] L. Kurvonen, J. T. Pulliainen, and M. T. Hallikainen, "Retrieval of Biomass in Boreal Forests from Multitemporal ERS-1 and JERS-1 SAR Images," *IEEE Trans. Geosci. Remote Sens.*, vol. 37, no. 1, pp. 198–205, 1999.
[7] J. T. Pulliainen, P. J. Mikkela, M. T. Hallikainen, and J.-P. Ikonen, "Seasonal Dynamics of C-Band Backscatter of Boreal Forests with Applications to Biomass and Soil Moisture Estimation," *IEEE Trans. Geosci. Remote Sens.*, vol. 34, no. 3, pp. 758–770, 1996.
[8] T. Nagler and H. Rott, "Retrieval of Wet Snow by Mean of Multitemporal SAR Data," *IEEE Trans. Geosci. Remote Sens.*, vol. 38, no. 2, pp. 754–765, 2000.
[9] M. S. Moran, D. C. Hymer, J. Qi, and E. E. Sano, "Soil moisture evaluation using multi-temporal synthetic aperture radar (SAR) in semiarid rangeland," *Agr. Forest Meteorol.*, vol. 105, pp. 69–80, 2000.
[10] S. Le Hgarat-Mascle, M. Zribi, F. Alem, A. Weisse, and C. Loumagne, "Soil Moisture Estimation from ERS/SAR Data: Toward an Operational Methodology," *IEEE Trans. Geosci. Remote Sens.*, vol. 40, no. 12, pp. 2647–2658, 2002.
[11] T. Kurosu, M. Fujita, and K. Chiba, "Monitoring of Rice Crop Growth from Space Using the ERS-1 C-band SAR," *IEEE Trans. Geosci. Remote Sens.*, vol. 33, no. 4, pp. 1092–1096, 1995.
[12] Y. Shao, X. Fan, H. Liu, J. Xiao, S. Ross, B. Brisco, R. Brown, , and G. Staples, "Rice monitoring and production estimation using multitemporal RADARSAT," *Remote Sens. Environ.*, vol. 76, no. 3, pp. 310–325, 2001.
[13] P. Lombardo, C. J. Oliver, T. Macrí Pellizzeri, and M. Meloni, "A New Maximum-Likelihood Joint Segmentation Technique for Multitemporal SAR and Multiband Optical Images," *IEEE Trans. Geosci. Remote Sens.*, vol. 41, no. 11, pp. 2500–2518, 2003.
[14] G. Camps-Valls, L. Gomez-Chova, J. Munoz-Mari, J. Rojo-Alvarez, and M. Martinez-Ramon, "Kernel-Based Framework for Multitemporal and Multisource Remote Sensing Data Classification and Change Detection," *IEEE Trans. Geosci. Remote Sens.*, vol. 46, no. 6, pp. 1822–1835, 2008.
[15] G. Davidson and K. Ouchi, "Segmentation of SAR images using multitemporal information," *IEE P. Radar Son. Nav.*, vol. 150, no. 5, pp. 367–374, 2003.
[16] L. Bruzzone, M. Marconcini, U. Wegmuller, and A. Wiesmann, "An Advanced System for the Automatic Classification of Multitemporal SAR Images," *IEEE Trans. Geosci. Remote Sens.*, vol. 42, no. 6, pp. 1321–1334, 2004.
[17] H. Skriver, F. Mattia, G. Satalino, A. Balenzano, V. Pauwels, N. Verhoest, and M. Davidson, "Crop Classification Using Short-Revisit Multitemporal SAR Data," *IEEE J. Sel. Topics Appl. Earth Observ.*, vol. 4, no. 2, pp. 423–431, 2011.
[18] F. Bovolo and L. Bruzzone, "A Detail-Preserving Scale-Driven Approach to Change Detection in Multitemporal SAR Images," *IEEE Trans. Geosci. Remote Sens.*, vol. 43, no. 12, pp. 2963–2972, 2005.
[19] P. Du, S. Liu, P. Gamba, K. Tan, and J. Xia, "Fusion of Difference Images for Change Detection Over Urban Areas," *IEEE J. Sel. Topics Appl. Earth Observ.*, vol. 5, no. 4, pp. 1076–1086, 2012.
[20] P. Gamba, F. Dell'Acqua, and G. Lisini, "Change Detection of Multitemporal SAR Data in Urban Areas Combining Feature-Based and Pixel-Based Techniques," *IEEE Trans. Geosci. Remote Sens.*, vol. 44, no. 10, pp. 2820–2827, 2006.
[21] Y. Bazi, L. Bruzzone, and F. Melgani, "An Unsupervised Approach Based on the Generalized Gaussian Model to Automatic Change Detection in Multitemporal SAR," *IEEE Trans. Geosci. Remote Sens.*, vol. 43, no. 4, pp. 874–887, 2005.
[22] J. Channussot, G. Mauris, and P. Lambert, "Fuzzy fusion techniques for linear features detection in multitemporal SAR images," *IEEE Trans. Geosci. Remote Sens.*, vol. 37, no. 3, pp. 1292–1305, 1999.
[23] G. Di Martino, A. Iodice, D. Riccio, G. Ruello, M. N. Papa, and Y. Koussoube, "Innovative Synthetic Aperture Radar Products for the Management of Land and Water," in *IEEE Global Humanitarian Technology Conf.*, 2012, pp. 117–121.
[24] L. Pulvirenti, M. Chini, N. Pierdicca, L. Guerriero, and P. Ferrazzoli, "Flood monitoring using multi-temporal COSMO-SkyMed data: Image segmentation and signature interpretation," *Remote Sens. Environ.*, vol. 115, pp. 990–1002, 2011.
[25] S. G. Dellepiane and E. Angiati, "A New Method for Cross-Normalization and Multitemporal Visualization of SAR Images for the Detection of Flooded Areas," *IEEE Trans. Geosci. Remote Sens.*, vol. 50, no. 7, pp. 2765–2779, 2012.
[26] J. Martinez and T. Le Toan, "Mapping of flood dynamics and spatial distribution of vegetation in the Amazon floodplain using multitemporal SAR data," *Remote Sens. Environ.*, vol. 108, no. 3, pp. 209–223, 2007.
[27] F. Siegert and A. A. Hoffmann, "The 1998 Forest Fires in East Kalimantan (Indonesia): A Quantitative Evaluation Using High Resolution, Multitemporal ERS-2 SAR Images and NOAA-AVHRR Hotspot Data," *Remote Sens. Environ.*, vol. 72, no. 1, pp. 64–77, 1998.
[28] C. Pohl and J. L. Van Genderen, "Multisensor image fusion in remote sensing: Concepts, methods and applications," *Int. J. Remote Sens.*, vol. 19, no. 5, pp. 823–854, 1998.
[29] D. Amitrano, G. Di Martino, A. Iodice, D. Riccio, G. Ruello, F. Ciervo, M. N. Papa, and Y. Koussoube, "Synthetic Aperture Radar for Humanitarian Purposes: Products and Opportunities," in *IEEE Global Humanitarian Technology Conf.*, 2013, pp. 546–551.
[30] U. Wegmüller and C. Werner, "Retrieval of Vegetation Parameters with SAR Interferometry," *IEEE Trans. Geosci. Remote Sens.*, vol. 35, no. 1, pp. 18–24, 1997.
[31] Agenzia Spaziale Italiana (ASI). COSMO-SkyMed SAR products handbook. [Online]. Available: http://www.cosmo-skymed.it/docs/ASI-CSM-ENG-RS-092-A-CSKSARProductsHandbook.pdf
[32] A. Torre, D. Calabrese, and M. Porfilio, "COSMO-SkyMed: Image quality achievements," in *Proc. 5th Int. Conf. Recent Advances Space Technologies*, 2011, pp. 861–864.
[33] S. Falzini and V. Speziale and E. De Viti, "COSMO-SkyMed active calibrator: A sophisticated tool for SAR image calibration," in *IEEE Int. Geosci. Remote Sens. Symp.*, 2007, pp. 1577–1580.
[34] D. Riccio, G. Di Martino, A. Iodice, Y. Koussoube, A. D. Pinelli, and G. Ruello, "Calibration of COSMO-SkyMed SAR data for hydrology applications," in *IEEE Int. Geosci. Remote Sens. Symp.*, 2012, pp. 844–847.

[35] D. D'Aria, A. Ferretti, A. Monti Guarnieri, and S. Tebaldini, "SAR Calibration Aided by Permanent Scatterers," *IEEE Trans. Geosci. Remote Sens.*, vol. 48, no. 4, pp. 2076–2086, 2010.

[36] A. Freeman, "SAR Calibration: an Overview," *IEEE Trans. Geosci. Remote Sens.*, vol. 30, no. 6, pp. 1107–1121, 1992.

[37] G. Di Martino, A. Iodice, A. Natale, D. Riccio, G. Ruello, I. Zinno, Y. Koussouben, M. N. Papa, and F. Ciervo, "COSMO-SkyMed AO Projects - Use of High Resolution SAR Data for Water Resource Management in Semi Arid Regions," in *IEEE Int. Geosci. Remote Sens. Symp.*, 2012, pp. 1212–1215.

[38] Z. Li and J. Bethel, "Image Coregistration in SAR Interferometry," in *Int. Archives Photogrammetry, Remote Sens. Spatial Information Services*, vol. XXXVII, 2008.

[39] M. J. D. Powell, "An efficient method for finding the minimum of a function of several variables without calculating derivatives," *Comput. J.*, vol. 7, no. 2, pp. 155–162, 1964.

[40] A. Ferretti, A. Monti Guarnieri, C. Prati, F. Rocca, and D. Massonnet, *InSAR Principles: Guidelines for SAR Interferometry Processing and Interpretation*. Postbus 229, 2200 AG Noordwijk: ESA Publications, ESTEC, 2007.

[41] G. Di Martino, M. Poderico, G. Poggi, D. Riccio, and L. Verdoliva, "Benchmarking Framework for SAR Despeckling," *IEEE Trans. Geosci. Remote Sens.*, vol. 52, no. 3, pp. 1596–1615, 2014.

[42] Trouvé, E. and Chambenoit, Y. and Classeau, N. and Bolon, P., "Statistical and operational performance assessment of multitemporal SAR image filtering," *IEEE Trans. Geosci. Remote Sens.*, vol. 41, no. 11, pp. 2519–2530, 2003.

[43] J. Bruniquel and A. Lopes, "Multi-variate optimal speckle reduction in SAR imagery," *Int. J. Remote Sens.*, vol. 18, no. 3, pp. 603–627, 1997.

[44] G. F. De Grandi, M. Leysen, J.-S. Lee, and D. Schuler, "Radar reflectivity estimation using multiple SAR scenes of the same target: technique and applications," in *IEEE Int. Geosci. Remote Sens. Symp.*, 1997, pp. 1047–1050.

[45] M. Ciuc, P. Bolon, E. Trouvé, V. Buzuloiu, and J. P. Rudant, "Adaptive neighborhood speckle removal in multitemporal SAR images," *Appl. Opt.*, vol. 40, no. 32, pp. 5954–5966, 2001.

[46] S. Quegan and T. Le Toan and J. J. Yu and F. Ribbes and N. Floury, "Multitemporal ERS SAR analysis applied to forest mapping," *IEEE Trans. Geosci. Remote Sens.*, vol. 38, no. 2, pp. 741–753, 2000.

[47] Y. Yu and S. Acton, "Speckle Reducing Anisotropic Diffusion," *IEEE Trans. Image Process.*, vol. 11, no. 11, pp. 1260–1270, 2002.

[48] e geos. COSMO-SkyMed Image Calibration. [Online]. Available: http://www.e-geos.it/products/pdf/COSMO-SkyMed-Image_Calibration.pdf

[49] P. Biancardi and L. Iannini and M. Mariotti d'Alessandro and A. Monti Guarnieri and S. Tebaldini, "Performances and limitations of Persistent Scatterers-based sar calibration," in *IEEE Radar Conference*, 2010, pp. 762–766.

[50] C. E. Shannon, "A mathematical theory of communication," *Bell Syst. Tech. J.*, vol. 27, pp. 379–423, 1948.

[51] D. Amitrano, G. Di Martino, A. Iodice, D. Riccio, G. Ruello, M. N. Papa, F. Ciervo, and Y. Koussoube, "Effectiveness of high-resolution SAR for water resource management in low-income semi-arid countries," *Int. J. Remote Sens.*, vol. 35, no. 1, pp. 70–88, 2014.

[52] A. K. Fung, "Scattering from a Vegetation Layer," *IEEE Trans. Geosci. Elect.*, vol. 17, no. 1, pp. 1–6, 1979.

[53] M. A. Karam, A. K. Fung, and Y. M. M. Antar, "Electromagnetic Wave Scattering from Some Vegetation Samples," *IEEE Trans. Geosci. Remote Sens.*, vol. 26, no. 6, pp. 799–808, 1988.

[54] Infoterra. Radiometric calibration of TerraSAR-X data. [Online]. Available: http://www2.astrium-geo.com/files/pmedia/public/r465_9_tsxx-itd-tn-0049-radiometric_calculations_i1.00.pdf.